nature communications

Article

https://doi.org/10.1038/s41467-025-67225-2

A disulfide redox switch mechanism regulates glycoside hydrolase function

Received: 29 March 2025

Accepted: 24 November 2025

Marcele Pandeló Martins[1], Gustavo Henrique Martins[1,2], Felipe Jun Fuzita[1], João Paulo Menezes Spadeto[1,3], Renan Yuji Miyamoto[1], Felippe Mariano Colombari[1], Fabiane Stoffel[1,2], Luciano Graciani Dolce[4], Camila Ramos dos Santos[1], Rodrigo Silva Araujo Streit[1], Antônio Carlos Borges[5], Rafael Henrique Galinari[6], Yoshihisa Yoshimi[6], Paul Dupree[6], Gabriela Felix Persinoti[1], Mariana Abrahão Bueno Morais[1] & Mario Tyago Murakami[1] ✉

Disulfide bonds are a key post-translational modification involved in protein folding, structural stability, and functional regulation. Here, we demonstrate that a glycoside hydrolase from the GH2 family undergoes reversible redox regulation through an intramolecular disulfide bond. The enzyme is inactive in its oxidized state and becomes active when reduced through a fully reversible process. Under oxidative conditions, multiple crystallographic and cryo-EM structures revealed a pronounced structural disorder in the active site, most prominent in the regulatory and catalytic loops, which disrupts the substrate binding site and, remarkably, the configuration of the acidic catalytic residues. Conversely, a high-resolution cryo-EM structure of the active (reduced) state unveiled a well-ordered active site with catalytic residues properly positioned for a classical Koshland retaining mechanism. This reversible order-disorder process based on a disulfide switch provides a mechanism for redox-dependent control of glycoside hydrolase activity, with potential implications for carbohydrate metabolism, microbial adaptation and biotechnological applications.

Proteins are remarkably sensitive to environmental modification, including variations in pH, temperature, ionic strength, and oxidative stress. Among these factors, the unique reactivity of sulfhydryl groups in cysteine residues allows reversible formation and disruption of disulfide bonds, in response to the redox environment[1]. This dynamic behavior underpins critical metabolic processes in biological systems, such as homeostasis[2,3], gene expression[4] and cellular signaling[5].

While the importance of cysteine residues in the metabolic regulation of proteins via reversible disulfide bonds is well documented, their role in carbohydrate enzymology is rather limited. To the best of our knowledge, cysteine residues are described to be functionally associated with (i) substrate recognition, observed in β-galactosidases *Arth*βDG[6] and KL-β-Gal[7]; (ii) coordination of non-catalytic metals, as described for the GH9 family[8]; (iii) coordination of catalytic metals in the families GH127[9] and GH146[10], where cysteine acts as a zinc-mediated nucleophile; and (iv) participation in a redox NAD$^+$-dependent catalytic mechanism in the GH4 family, where a reduced cysteine in the second coordination sphere with substrate coordinate a divalent metal that interacts with both NAD$^+$ and substrate[11].

---

[1] Brazilian Biorenewables National Laboratory (LNBR), Brazilian Center for Research in Energy and Materials (CNPEM), Campinas, São Paulo, Brazil. [2] Graduate Program in Molecular and Morphofunctional Biology, Institute of Biology, University of Campinas, Campinas, São Paulo, Brazil. [3] Graduate Program in Chemistry, Institute of Chemistry, University of Campinas, Campinas, São Paulo, Brazil. [4] Institute for Advanced Biosciences (IAB), INSERM U1209, CNRS UMR 5309, Université Grenoble-Alpes, Grenoble, France. [5] Brazilian Nanotechnology National Laboratory (LNNANO), Brazilian Center for Research in Energy and Materials (CNPEM), Campinas, São Paulo, Brazil. [6] Department of Biochemistry, University of Cambridge, Cambridge, MA, USA.
✉ e-mail: mario.t.murakami@gmail.com

Cysteines in Carbohydrate-Active enZymes (CAZymes) also form disulfide bonds that play a critical role in structural stabilization, including maintaining protein folding and enhancing thermostability. This is exemplified by cellulases from the families GH5[12], GH12[13], and GH45[14], a GH11 xylanase[15], and lysozymes from the families GH22[16] and GH24[17]. Despite their extensive occurrence, the regulatory potential of disulfide bonds in CAZymes remains undescribed. To date, no studies have addressed whether reversible disulfide bond dynamics contribute to redox-sensitive regulation in these enzymes, leaving a gap in understanding how CAZymes might adapt to oxidative environments and the molecular mechanisms enabling such adaptation.

In this work, by employing an integrative approach including synchrotron X-ray crystallography, single-particle cryo-EM, molecular dynamics simulations, site-directed mutagenesis, enzyme kinetics and mass spectrometry, we uncover a distant GH2 member, whose activity is reversibly regulated by a redox switch involving an intramolecular disulfide bond. Our findings demonstrate that this glycoside hydrolase undergoes reversible disulfide bond formation between two cysteine residues located in the catalytic interface. The oxidized enzyme exhibits a conformational disorder in the active site (regulatory and catalytic loops) that impair enzymatic activity, while reduction promotes active site reorganization, leading to maximum catalytic function. Acting as a regulatory switch, this reversible disulfide bond enables the enzyme to respond dynamically to changes in oxidative environments while simultaneously offering protection against irreversible oxidative damage. These findings expand our current understanding of redox-mediated regulation via disulfide bonds in CAZymes, providing opportunities to explore their functional roles in cellular processes and under oxidative stress conditions.

Results

A redox-regulated glycoside hydrolase

The exploration of the genetic landscape from microbial life specialized in plant biomass deconstruction from Brazilian biodiversity has been demonstrated to be an untapped source of unique enzymatic systems, including several recently discovered CAZy families, such as AA18[18], GH173[19], CBM89[19], and CE20[20].

Mining metagenome-assembled genomes (MAGs) recovered from Brazilian biodiversity, we discovered an uncharacterized bacterium, named 'Candidatus Capybacter oxireducens' that harbors a distant GH2 member (CapGH2b) that co-localizes with mannan-active enzymes belonging to GH173 and GH5_57 families (Fig. 1a). Sequence similarity analysis (SSN) revealed that this member along with other GH2 sequences, predominantly from gut microbiota Bacteroidales, establishes an uncharacterized cluster (UC) within this family (Fig. 1b, Supplementary Fig. 1). According to the recent classification proposed by the CAZy team, this cluster, based on sequence similarity, would belong to the GH2_13 subfamily[21]. To gain insights into the function of this UC, we produced and performed the biochemical characterization of recombinant CapGH2b, confirming its β-mannosidase activity (Supplementary Fig. 2), which supports the genomic context along with other mannan-active enzymes.

To further evaluate the enzyme responsiveness to ligands, assays were conducted in the presence of monosaccharides, metals, and reducing agents. As expected, mannose had a negative impact on enzyme activity as well as other monosaccharides and distinct metals, including Co^{2+}, Ni^{2+}, Cu^{2+}, Zn^{2+}, and Fe^{2+} (Supplementary Fig. 2). The presence of EDTA had no effect, indicating that CapGH2b is not a metal-dependent enzyme. Interestingly, an increase in the catalytic activity was observed upon incubation with DTT, suggesting that the enzyme would be responsive to reducing agents (Fig. 1c).

To further explore this unusual redox behavior, a mild oxidizing condition was employed, utilizing atmospheric oxygen during long-term incubation, which led to an enzymatic activity decrease of 90% (Fig. 1c). Subsequent treatment of the oxidized enzyme with varying DTT concentration and incubation times restored the enzymatic activity, and even enhanced compared to its initial levels (Fig. 1d). All tested DTT concentrations resulted in similar maximum activity values (~100 U g^{-1}), indicating saturation of catalytic activity (Fig. 1d). The recovery of activity with DTT treatment supports a putative reversible redox-dependent regulatory mechanism.

To investigate oxidation over a shorter timescale, the enzyme was treated with the oxidizing agent H_2O_2, followed by incubation with DTT as a reducing agent. The enzyme demonstrated a behavior consistent with long-term atmospheric oxidation, confirming that oxidation can be chemically induced and subsequently reversed by reducing treatments (Fig. 1e–h, Supplementary Figs. 3, 4). However, as H_2O_2 concentrations increase, the activity recovery decreases, suggesting that higher levels of H_2O_2 result in irreversible and non-specific oxidation processes, impairing the full enzymatic activity reestablishment.

After enzyme treatment with H_2O_2 or DTT, thermostability assays were performed to evaluate whether oxidation and reducing processes can influence structural stability (Supplementary Fig. 5). No remarkable difference in thermostability was observed in the enzyme incubation with H_2O_2 or DTT, indicating that the redox mechanism does not influence the enzyme thermostability but appears to specifically regulate enzymatic activity.

These findings underscore an unprecedented redox regulatory mechanism for carbohydrate breakdown, in which oxidation impairs activity, whereas reduction effectively restores enzymatic activity, making it a fully reversible process.

The inactive conformation exhibits a disordered active site

To elucidate the structural basis for this redox regulation, we determined the enzyme structure using X-ray crystallography via the single-wavelength anomalous dispersion (SAD) method (Supplementary Table 1). The CapGH2b structure retains the conserved modular architecture typical of GH2 enzymes, comprising five domains (Supplementary Fig. 6). However, the domain 5 in CapGH2b lacks the β-sandwich fold and is consequently shorter than in other GH2 members (Supplementary Fig. 6). This truncated domain likely influences oligomerization[22] and could potentially alter the enzyme assembly properties. Indeed, crystal packing analysis revealed a homotrimeric organization of CapGH2b, further confirmed in solution by SEC-MALS and SAXS (Supplementary Fig. 7), which contrasts with other structurally characterized family members featuring a homodimeric organization, such as *Bt*Man2A[22] and *Dt*Man[23].

Unexpectedly, the refined structure revealed a massive structural disorder in the catalytic domain, specifically in two major loops of the catalytic interface, named here as catalytic (G462-P482) and regulatory (S509-G536) loops (Fig. 2a). These loops contribute to defining the topology of the active site and contain key residues for substrate anchoring (N464 and W532) and catalytic activity (acid/base E465). However, their intrinsic flexibility precludes the visualization of electron density and, therefore, the active site configuration, indicating that this disordered structure likely corresponds to the inactive conformation.

In an effort to obtain the structured active site, the enzyme was crystallized in ten different conditions, featuring distinct space groups and molecules content within the asymmetric units (Supplementary Fig. 8, Supplementary Tables 1, 2). However, in all structures, consistently, the active site was disordered, in particular these two loops. Mass spectrometric analysis of crystallized samples revealed the presence of the full-length protein (Supplementary Table 3), discarding the possibility of the absence of electron density is due to internal protein cleavage by endogenous proteolytic activity. It reiterates that these loops are inherently disordered regions in the captured conformational state of the enzyme by X-ray crystallography, as also predicted by FoldIndex[24] (Supplementary Fig. 9).

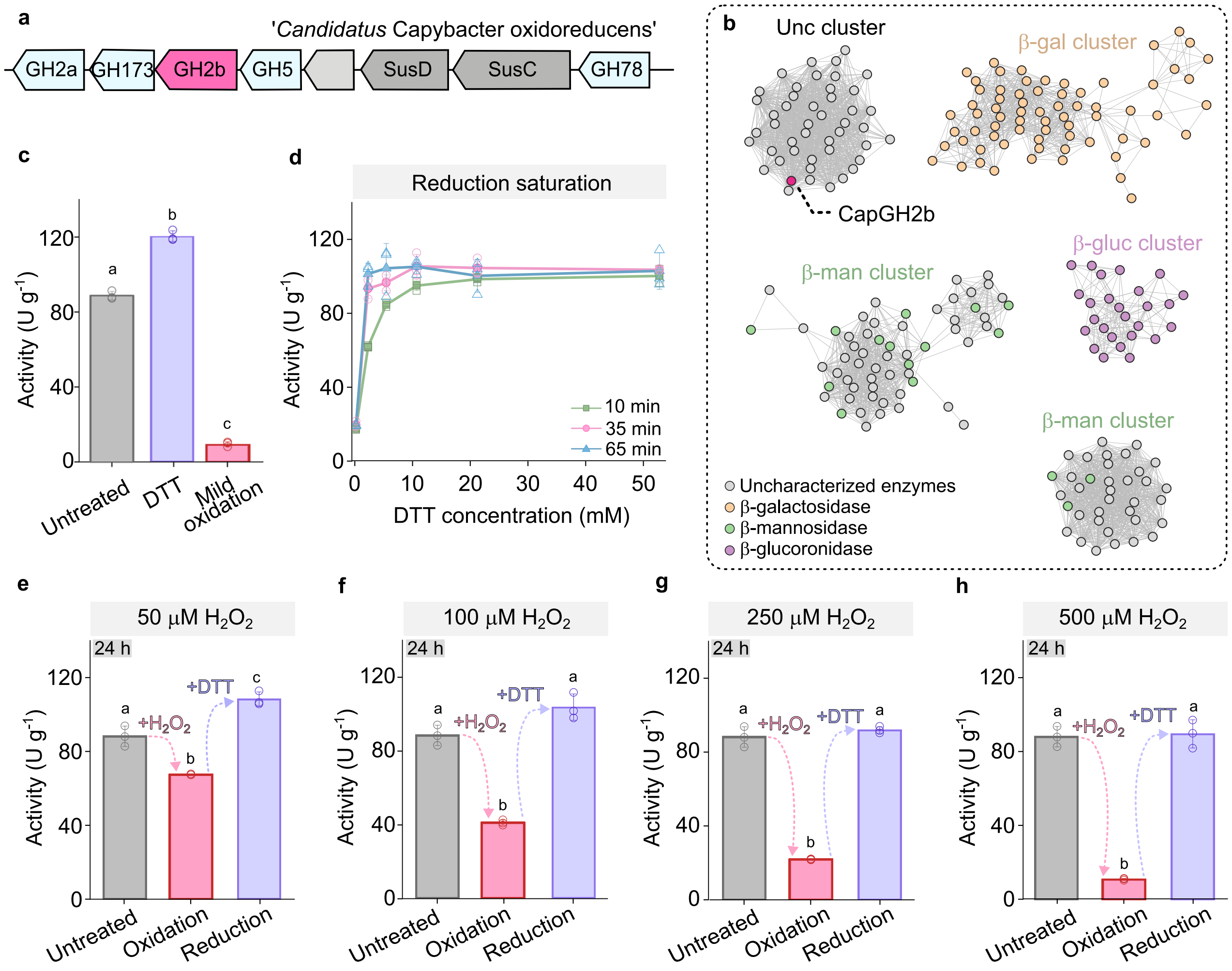

Fig. 1 | CapGH2b is catalytically active under reducing conditions and inactive upon oxidation. a Genetic organization of the β-heteromannan Polysaccharide Utilization Locus (PUL) from '*Candidatus* Capybacter oxireducens', identified in the capybara gut microbiome. **b** Sequence similarity network (SSN) analysis of CapGH2b and its closest orthologs from CAZy and Uniprot. Functionally characterized enzymes are colored according to their activity and organized into clusters. **c** Enzymatic activity assay showing that the fresh enzyme (untreated) is active under reducing conditions (20 mM DTT incubation), while mild oxidation (long-term incubation at 4 °C) leads to activity reduction. **d** Reduction saturation curve with the post-mild oxidation enzyme incubated under different DTT concentrations and time points. Maximum activity restoration upon DTT treatment confirms reversible redox regulation. **e,f** H_2O_2-induced oxidation over 24 hours at different concentrations progressively diminishes enzymatic activity. Subsequent DTT treatment fully restores activity, supporting a redox-sensitive regulatory mechanism. All results represented in (**c**–**h**) are expressed as mean ± standard deviations from three independent experiments ($n = 3$). The statistical significances in (**c**, **e**–**h**) were determined by one-way ANOVA with Tukey's post hoc test ($p < 0.001$), and bars sharing the same letter in each panel do not present statistically significant difference. Source data and exact p-values are provided as a Source Data file.

Our extensive attempts to resolve the crystal structure with ordered loops were unsuccessful, suggesting that the observed disorder may be related to the oxidation process. The typical incubation time and temperature used for crystallization likely favor oxidation, leading to its inactive state. This hypothesis is supported by the disordered active site observed in all crystal structures and aligns with biochemical data demonstrating that the oxidized state is catalytically inactive. Therefore, the crystallization process itself appears to hinder the elucidation of the active conformation.

The ordered active conformation

To overcome the technical limitations imposed by the crystallization process to solve the active conformation of the enzyme, we employed high-resolution single-particle cryo-EM. In this approach, fresh protein preparations exhibiting full catalytic activity were rapidly vitrified, ensuring the active conformation of the enzyme. The cryo-EM structure achieved a high global resolution of 2.6 Å, which allowed the visualization of side chains throughout the trimeric biological unit (Fig. 2b, Supplementary Figs. 10, 11, and Supplementary Table 4). Remarkably, the two flexible (catalytic and regulatory) loops in all crystallographic structures presented a well-defined conformation in the active state captured by cryo-EM. In this structure, we were able to unambiguously identify key residues for catalysis, including the acid/base E465, the catalytically relevant N464, and the +1 aromatic residue W532 (Fig. 2b). To discard that the crystallographic structures featuring disrupted active site is not a crystallization artifact, we also solved the oxidized structure of CapGH2b by cryo-EM. Similar to crystallographic structures, both catalytic and regulatory loops were not observed, supporting their intrinsic disorder in the oxidized (inactive) state (Fig. 2a,c, Supplementary Figs. 10, 11, Supplementary Table 4).

The active conformation of the enzyme revealed that both the catalytic and regulatory loops are essential for defining the architecture of the active site, principally the +1 subsite (Fig. 2d). Interestingly, CapGH2b contains two glycine residues (G473 and G533 in the catalytic and regulatory loops, respectively), which results in an opened active-site pocket architecture compared to structurally

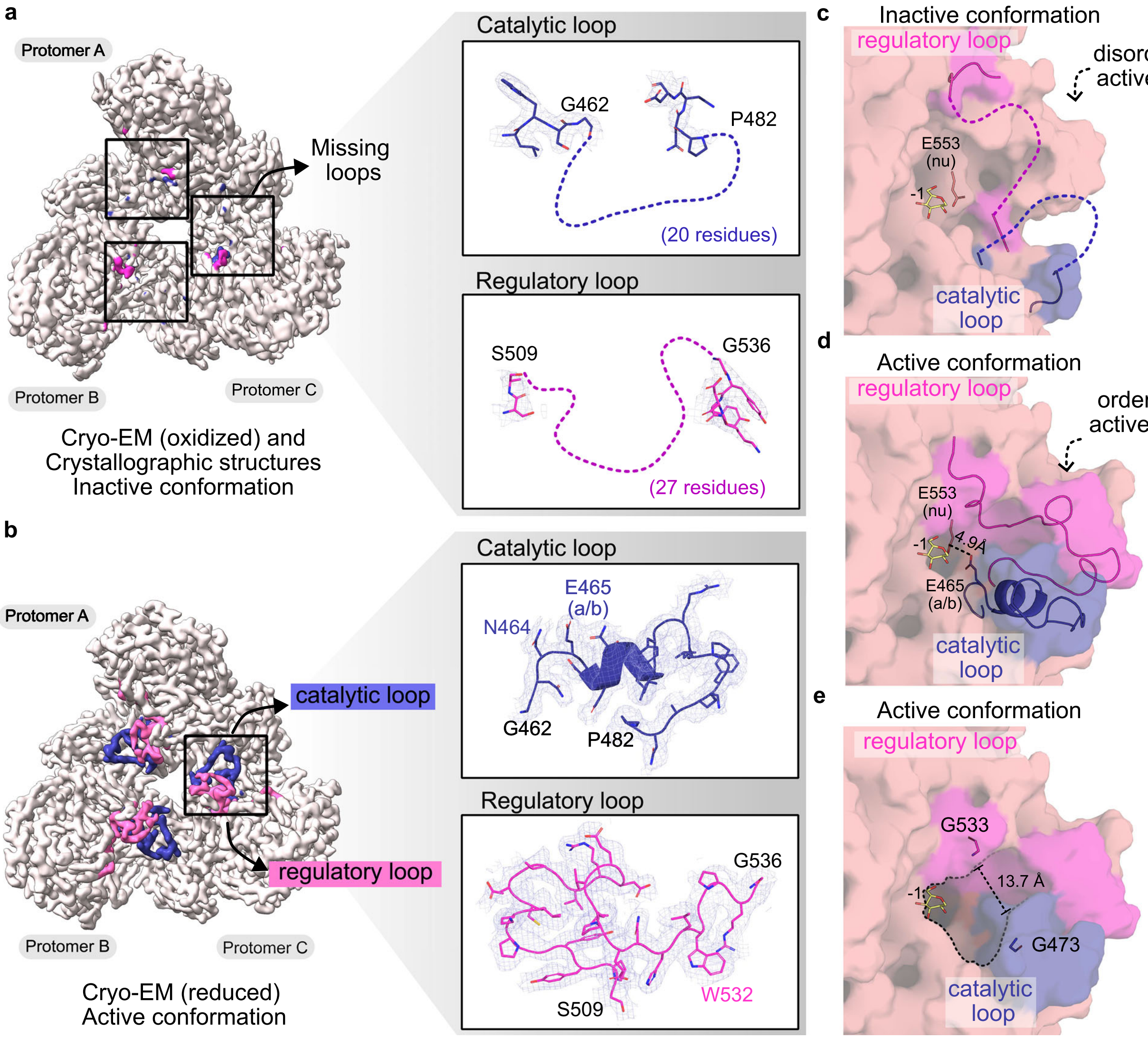

Fig. 2 | Structural order/disorder transitions in the active site drive active/inactive conformations. a Structural disorder of the catalytic and regulatory loops in the active site observed in oxidized samples via crystallography and cryo-EM. The left panel shows the cryo-EM map (deepEMhancer, contoured at a level of 0.11), while the middle panel shows the corresponding crystallographic electron density maps (contoured at 1.0σ). **b** Ordered conformation of the loops, captured by cryo-EM of fresh samples (predominantly in the reduced form), with the deepEMhancer map represented at a 0.20 level. **c** Loops disorder leads to enzyme inactivation by disrupting active site architecture, preventing the catalytic acid/base E465 visualization. **d** Loops ordering restores the structural integrity of the active site and properly positions catalytic residues, enabling substrate processing via a Koshland double-displacement mechanism. **e** CapGH2b features an open +1 subsite, distinct from its orthologs (Supplementary Fig. 12), which is shaped by catalytic and regulatory loops. The mannose positioned in the −1 subsite of (**c**–**e**) was obtained by structural superposition with *Dt*Man (PDB 5N6U[23]). Residues from catalytic and regulatory loops are colored deep blue and light magenta, respectively.

characterized GH2 members (Fig. 2e, Supplementary Fig. 12). In those structures, the corresponding residue to G473 is W465 in *Dt*Man (PDB 5N6U[23]), W470 in *Bt*Man2A (PDB 2JE8[22]) and W485 in XacMan2A (PDB 6BYE[25]), which serves as a hydrophobic platform for sugar anchoring in the +1 subsite (Supplementary Fig. 12). The next glycine residue in the regulatory loop (G533) corresponds to H490 in *Dt*Man[23], Y537 in *Bt*Man2A[22], and G557 in XacMan2A[25], which also contribute to the +1 subsite topology. Supporting this, the opened +1 subsite of CapGH2b does not impose a steric barrier for accommodating distinct substrate orientations (Supplementary Fig. 12). This adaptability suggests the capacity of the enzyme to recognize and process branched mannooligosaccharides, similar to the role of the co-localized enzyme, CapGH5_57, in cleaving branched hetero-β-mannans[26].

Remarkably, the lack of key aromatic residues in the catalytic loop seems to be compensated by the presence of W532 in the regulatory loop. Ligand docking analysis indicates that this residue serves as a hydrophobic platform for the +1 glycoside and forms a hydrogen bond with O5 from mannose in the −1 subsite (Supplementary Fig. 12). Additionally, the residue R535, also located in the regulatory loop, establishes hydrogen bonds with the +1 sugar moiety (Supplementary Fig. 12), an interaction in this subsite not previously reported for GH2 members. These analyses reveal the extensive structural remodeling of the +1 subsite in CapGH2b, driven by the unique molecular properties of both catalytic and regulatory loops.

Following the atypical molecular pattern observed in the +1 subsite, the −1 subsite also exhibits a previously undescribed configuration, featuring I201 and D670 in positions typically occupied by tryptophan residues in all structurally characterized orthologs (Supplementary Figs. 12, 13). Molecular docking analysis indicates that the loss of polar interactions between mannose and the NH of the corresponding tryptophan, which is replaced by I201, is compensated by the presence of the non-conserved residue R605. Moreover, D670 plays a key role in positioning R605, along with R535, which also forms a hydrogen bond with mannose in the −1 subsite of CapGH2b

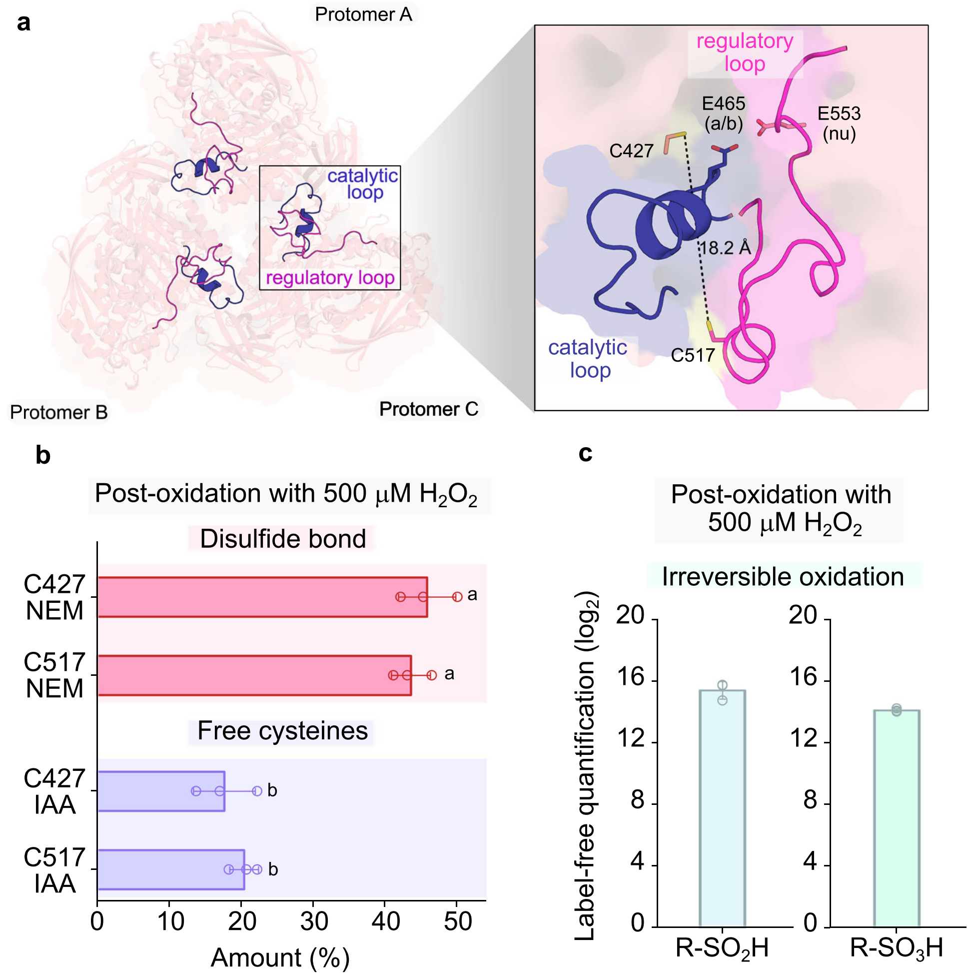

Fig. 3 | Structural flexibility of catalytic and regulatory loops enables disulfide bond formation between C427 (in the active site) and C517 (in the regulatory loop). a The cysteine pair C427 and C517 are 18.2 Å apart in the reduced state, with the catalytic loop creating a steric barrier between them. The catalytic residues comprising the acid/base E465 and the nucleophile E553 are shown. **b** Relative percentages of C427 and C517 involved in disulfide bond formation (labeled with NEM) or remaining in the free state (labeled with IAA), determined post-oxidation with 500 μM H_2O_2, based on standard curves. Results are expressed as mean ± standard deviations from three independent experiments ($n = 3$). Each quantification value corresponds to the median of nine technical replicate injections monitoring two fragment ions, as detailed in Supplementary Table 5. The statistical significance was determined by one-way ANOVA with Tukey's post hoc test ($p < 0.001$), and bars sharing the same letter do not present statistically significant difference. **c** Quantification of irreversible overoxidized species (-SO_2H and -SO_3H) at C427 post-oxidation with 500 μM H_2O_2. These oxidized peptides were not detected in the reduced control samples. Results are expressed as mean ± standard deviations from three independent experiments ($n = 3$). Source data and exact *p*-values are provided as a Source Data file.

(Supplementary Figs. 12, 13). These structural adaptations in both the negative and positive subsites of CapGH2b underpin an unprecedented molecular basis for substrate recognition within the GH2 family.

Regarding the catalytic residues in the active conformation, the nucleophile and the acid/base are productively positioned with a distance of 4.9 Å (Fig. 2d), similar to that observed in structurally characterized GH2 members, such as *Dt*Man, *Bt*Man2A, XacMan2A, and *Th*Man2A (PDBs 5N6U[23], 2JE8[22], 6BYE[25] and 4CVU[27], respectively). Therefore, despite a substantial remodeling of both −1 and +1 subsites in the active conformation, the Koshland retaining catalytic mechanism is conserved.

Intramolecular disulfide bond formation

The determination of both active (reduced) and inactive (oxidized) conformations shed light on a redox order-disorder process controlling the catalytic activity, remaining yet unclear the residues involved in this process. A detailed structural inspection of the active conformation revealed two free cysteines exposed to the solvent, potentially capable of forming a disulfide bond, C427 and C517, both located at the catalytic interface (Supplementary Fig. 14). C427 is in the vicinity of the active site, whereas C517 is located in the intrinsically flexible regulatory loop. In the active conformation, these residues are approximately 18 Å apart, with the catalytic loop localized between them, imposing a steric barrier for disulfide bond formation (Fig. 3a). Notably, in the inactive structure this physical barrier imposed by the catalytic loop is not present due to the flexibility observed for catalytic and regulatory loops (Fig. 2a). This massive disorder of the catalytic interface in the oxidized state makes feasible the intramolecular disulfide bond formation between these residues. Further support comes from the observation of a continuous electron density emerging from the cysteine C427 side chain in some crystallographic structures and cryo-EM of the oxidized enzyme, suggesting its potential involvement in the formation of a covalent interaction (Supplementary Fig. 15).

The possibility of an intermolecular disulfide bond in the trimeric arrangement was also verified; however, the distance between C427 in adjacent protomers is ~47 Å (Supplementary Fig. 16). The best chance for an intermolecular disulfide bond is between two neighboring C517 residues, which are yet approximately ~24 Å apart (Supplementary Fig. 16). However, the comparison of both active and inactive structures did not reveal any structural rearrangements that would favor the C517-C517 disulfide bond formation. Therefore, the most plausible hypothesis in light of the structural data is the formation of an intramolecular disulfide bond between C427 and C517, both of which are located in the catalytic interface.

To confirm this interpretation, we employed targeted proteomics to identify and quantify peptides containing these cysteine residues, in both free and covalently bonded states, using a differential cysteine labeling strategy based on the use of two distinct alkylating agents. Free cysteines were labeled with iodoacetamide (IAA) in non-reduced samples, while covalently bonded cysteines were selectively labeled, after reduction, with *N*-ethylmaleimide (NEM). In the reduced enzyme control, C427 and C517 were primarily identified in their free state. In contrast, the oxidized enzyme predominantly showed C427 and C517 covalently bonded to NEM with similar quantitative values, indicating disulfide bond formation between these residues (Fig. 3b, Supplementary Figs. 17, 18, Supplementary Table 5). Some cysteine residues remained in the free state after oxidation (Fig. 3b), which correlates with the residual activity observed post-oxidation (Fig. 1h). Additionally, the total proportion of free and oxidized cysteines reached approximately 60%, indicating the presence of irreversible oxidizing modifications in cysteine residues caused by the exogenous oxidizing agent (500 μM H_2O_2). These modifications include the formation of sulfinic ($-SO_2H$) and sulfonic ($-SO_3H$) acid species confirmed by mass spectrometry (Fig. 3c, Supplementary Fig. 19).

The redox switch mechanism

To further validate this model, we next evaluated the role of these cysteine residues in the redox-dependent activity regulation by site-directed mutagenesis. Interestingly, the incubation of the C517A variant with DTT resulted in minimal changes in activity (Supplementary Fig. 20), revealing that the absence of this thiol side chain makes the enzyme unresponsive to redox changes. Furthermore, the activity levels of the C517A variant are similar to the wild-type enzyme, indicating that this residue does not directly contribute to the catalytic process but serves as a regulatory element. To assess the oxidation profile, the variant C517A was subjected to mild oxidizing conditions, as in the WT enzyme. Under mild oxidation, the C517A variant exhibited minimal changes in activity, even after DTT treatment, a distinct behavior compared to the WT enzyme (Fig. 4a, Supplementary Fig. 20). This implies that the C517A variant is "locked" in the active conformation, being insensitive to redox changes.

Docking analysis revealed that the cysteine residue C427 makes critical hydrogen bonds at the −1 subsite with O3 from mannose, NH from N464, and OE1 from the acid/base residue E465 (Supplementary Fig. 21). These interactions play a pivotal role in enzymatic activity involving substrate binding, contributing to the correct acid/base positioning for catalysis, and the interaction with N464 further stabilizes the sugar transition state during hydrolysis[22]. Consequently, as expected, the C427A variant exhibited an expressive reduction in activity (Supplementary Fig. 21). Despite its low residual activity, the C427A variant still exhibited partial responsiveness to redox changes, suggesting that oxidation of C517 favors a structural shift towards the disordered (inactive) state, which could facilitate disulfide bond formation (Supplementary Fig. 22). In contrast, the C427A/C517A double mutant was completely insensitive to redox treatments, even under high peroxide concentrations (500 μM), confirming that redox-dependent modulation of activity is mediated by the residues C427 and C517 (Supplementary Fig. 22).

The use of a strong oxidizing agent (H_2O_2) had a remarkable reduction in the catalytic activity of the variant C517A, and contrary to WT, DTT treatment failed to restore enzymatic activity (Fig. 4b, Supplementary Figs. 23, 24). This indicates an irreversible process mediated by unspecific oxidation events involving the peptide containing C427, evidenced by its low recovery post-oxidation (Supplementary Fig. 25, Supplementary Table 6). Additionally, a considerable formation of overoxidized C427 species, including sulfinic ($-SO_2H$) and sulfonic acids ($-SO_3H$), was observed 6-fold and 7.5-fold higher, respectively, compared to the WT enzyme (Fig. 4c). This result also highlights a potential shielding effect provided by the intramolecular disulfide bond formation, preventing irreversible oxidative damage of the catalytically relevant cysteine residue. Protective disulfide bonds were previously described[2,28], acting as a mechanism to shield proteins from irreversible oxidative damage by enabling a reversible redox process that preserves function under oxidative stress.

The negative impact of the disulfide bond between C427 and C517 on activity was further demonstrated through molecular dynamics simulations of the oxidized state. The intramolecular disulfide bond prevents C427 from interacting with the substrate and induces a prominent steric hindrance for substrate binding (Supplementary Fig. 26). Additionally, the optimal catalytic distances between key residues are disrupted, increasing to over 14 Å (Supplementary Figs. 26, 27). These data highlight how protein oxidation alters the structural and functional dynamics of the active site, thereby modulating enzymatic activity.

Compared to C427, C517 is more solvent exposed (31% vs 13%) and has a markedly lower predicted pKa (10.3 vs. 15.1)[29], indicating it is more prone to initial oxidation. Therefore, we suggest that deprotonation/oxidation of C517 destabilizes the ordered conformation, favoring regulatory loop flexibility, which in turn contributes to the formation of the disulfide bond between C427 and C517.

The proximity of the regulatory loop to the oligomeric interface further raises the possibility that disulfide bond formation could also influence oligomer stability. To test this, we compared the oligomeric states of WT, C517A, and C427A under oxidative and reductive conditions. The WT enzyme exhibited a concentration-dependent, reversible shift from trimer to monomer upon H_2O_2 treatment, whereas both variants remained exclusively trimeric (Supplementary Fig. 28). These results indicate that once a disulfide bond is formed, structural disorder is propagated to other regions, including the oligomeric interface. This perturbation of the oligomeric arrangement is supported by changes in electrostatic and hydrogen-bonding interactions near the oligomeric interface upon disulfide bond formation (Supplementary Fig. 29).

Taking together, these findings support a reversible redox-regulated mechanism in which the inherent flexibility of the regulatory loop, which can be further favored by C517 oxidation, facilitates the formation of an intramolecular disulfide bond between C427–C517 locking the enzyme in a disordered and inactive conformation. This mechanism might have implications in controlling the enzyme activity under environmental redox changes and as a protein protective effect against oxidative stress.

Discussion

Proteins have evolved a plethora of molecular mechanisms to adapt and control their functions in response to environmental changes. Central to these adaptive strategies are disulfide bonds, whose increased occurrence has been associated with the emerging complexity of living systems[30], highlighting their evolutionary importance. In carbohydrate breakdown and metabolism, the role of disulfide bonds is yet underexplored, predominantly associated with maintaining tertiary structure, enhancing thermostability or facilitating proper folding[12–17].

In this work, we demonstrated a reversible redox switch mechanism that regulates a glycoside hydrolase from the gut microbiota. The enzyme is inactive under oxidizing conditions, but its full catalytic activity is restored upon reduction (Fig. 5). Biochemical and structural data confirmed the presence of a reversible disulfide bond between C427 and C517 (located in the catalytic and regulatory loops,

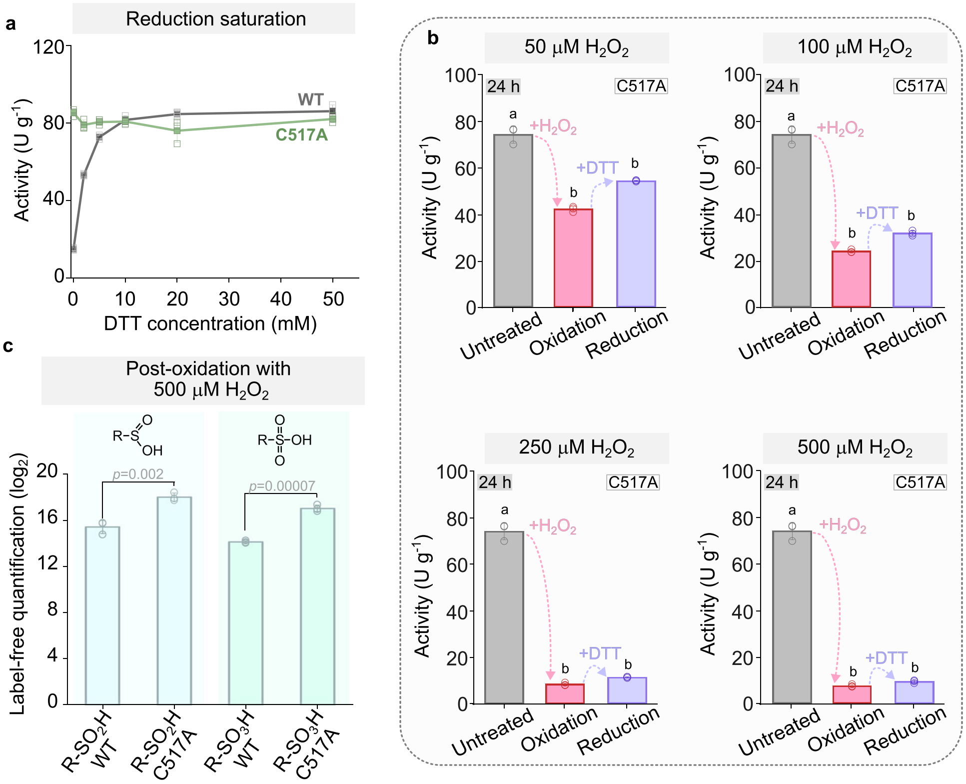

Fig. 4 | C517A variant is unresponsive to reducing agents. a Reduction saturation assessment of the C517A variant post-mild oxidation, incubated under different DTT concentrations for 10 min. Unlike the WT enzyme, the C517A variant maintained a constant activity profile across different DTT concentrations, indicating insensitivity to reducing agents. Results are expressed as mean ± standard deviations from three independent experiments ($n = 3$). **b** Enzymatic activity detection of C517A after H_2O_2-induced oxidation over 24 hours at different H_2O_2 concentrations, following DTT treatment. Oxidation led to a decrease in enzymatic activity, and subsequent reduction treatment was unable to recover the initial activity, indicating an irreversible redox regulation mechanism, unlike the WT enzyme. Results are expressed as mean ± standard deviations from three independent experiments ($n = 3$). The statistical significance was determined by one-way ANOVA with Tukey's post hoc test ($p < 0.001$), and bars sharing the same letter in each panel do not present statistically significant difference. **c** Label-free quantification of C427 irreversible oxidation to sulfinic (-SO_2H) and sulfonic acids (-SO_3H), assessed post-oxidation with 500 μM H_2O_2, detected by proteomics. Results are expressed as mean ± standard deviations from three independent experiments ($n = 3$). A two-sample Student's t-test comparing label-free quantification values revealed significantly higher sulfinic and sulfonic acid levels in the C517A variant, supporting the protective role of the disulfide bond in the WT enzyme. These oxidized peptides were not identified in the reduced control samples. Source data and exact p-values are provided as a Source Data file.

respectively), underlining an unprecedented regulatory role in carbohydrate enzymology.

Cryo-EM analysis of the reduced (active) structure revealed that C427 and C517 are 18 Å apart, with the catalytic loop acting as a steric barrier between them. This spatial configuration suggests that disulfide bond formation requires massive conformational rearrangements, as corroborated by the flexible and disordered nature of these two loops observed in oxidized structures. This phenomenon aligns with other redox-regulated proteins where structural flexibility facilitates disulfide bond formation. For instance, in CLIC1, C24 and C59 located 13 Å apart, require the local unfolding of one α-helix and four β-strands into loops to form the disulfide bond[31,32]. Similarly, in *Ae*bcp, C49 and C54, separated by 10.6 Å in the reduced form, undergoes a conformational change involving helix disruption and β-hairpin formation upon oxidation[31,33]. A similar order-to-disorder transition is observed in the SARS-CoV main protease (M^{pro}), where oxidation of the catalytic cysteine C145, located 8 Å from C117, disrupts a β-hairpin motif and drives disulfide bond formation[34,35].

However, typical order-disorder mechanisms linked to redox regulation reported in the literature involve structural ordering upon disulfide bond formation. For instance, in the reduced state of PRD1, C254 is located within a flexible region (248-269), and upon oxidation and disulfide bond formation between C254 and C277, this region becomes structured[31,36]. Similarly, in *Ac*gdhB, C338 and C345 become visible only when stabilized by disulfide bond formation, transitioning from a flexible loop in the reduced form to a helical structure in the oxidized state[31,37,38]. In CapGH2b, the process is inverse, in which the formation of the disulfide bond favors local disorder, impairing enzyme function. Although unconventional, a similar case was reported for the protein *Tt*Leu-tRNA, in which the reduced state exhibits an ordered β-hairpin arrangement, whereas the oxidized state displays a disruption of this secondary structure caused by a disulfide bond between C439 and C484 that prevents zinc binding[31,39,40]. These observations highlight the critical role of structural flexibility and dynamic rearrangements across diverse proteins in a bidirectional way involving order-disorder processes and disulfide bond formation.

This mechanism identified in CapGH2b may extend to its closest orthologs that conserve the cysteine pair (Supplementary Fig. 30) and display comparable intrinsic flexibility in the corresponding regulatory loop (Supplementary Fig. 31). These two features are critical for redox-responsive disulfide bond formation. Notably, these orthologs are predominantly recovered from gut and fecal microbiota of diverse animal hosts, especially within the genus *Alistipes* (phylum Bacteroidota), suggesting that the redox-regulatory mechanism uncovered in CapGH2b might be functionally relevant within gut-associated microbial communities.

Furthermore, CapGH2b and its closest orthologs are predicted to be intracellular proteins (periplasmic or cytoplasmic)[41], consistent with the observation that CapGH2b does not act on polymeric substrates. Within the Bacteroidota phylum, multiple steps of carbohydrate

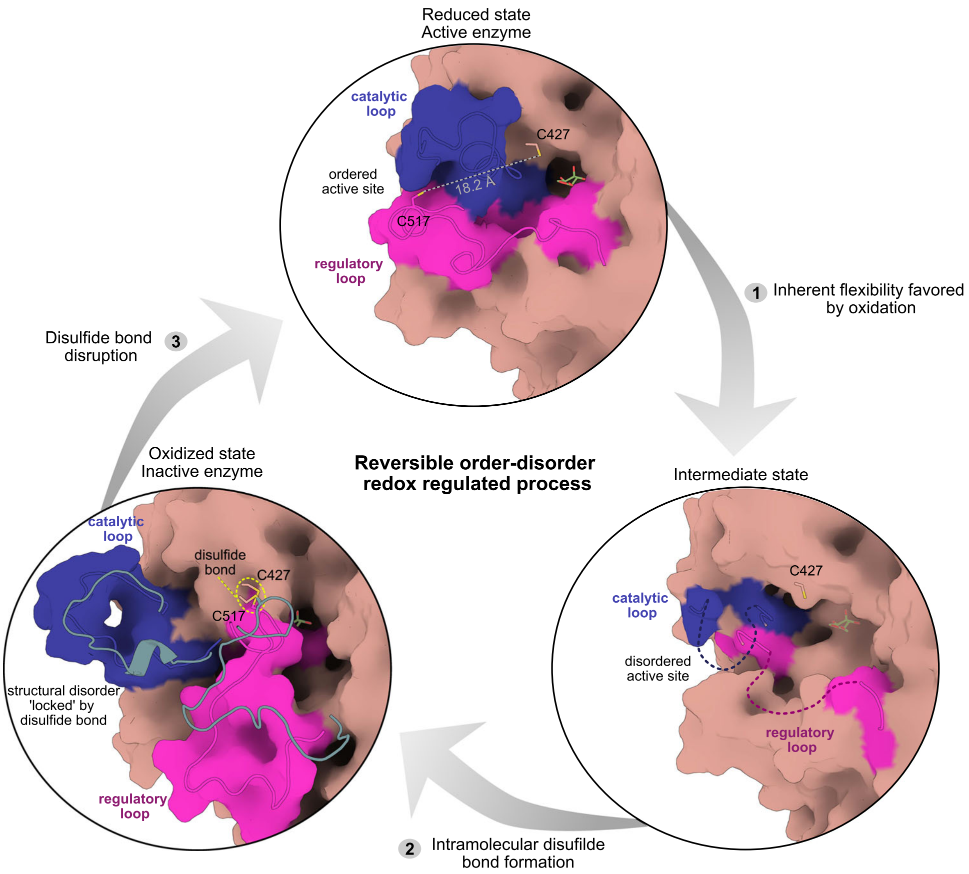

Fig. 5 | The reversible order-disorder redox mechanism. In the reduced state, the enzyme adopts an active conformation, with C427 and C517 positioned 18.2 Å apart, separated by the catalytic loop. This structural arrangement maintains active site integrity, allowing proper substrate binding and catalysis. Upon oxidation, C527 can be initially deprotonated/oxidized, favoring the intrinsic flexibility of the regulatory loop, defining a disordered intermediate state. This conformational change disrupts the active site architecture, impairing substrate recognition. This favored flexibility facilitates disulfide bond formation between C427 and C517, locking the enzyme in the inactive (disordered) state. A second structural snapshot from molecular dynamics simulations (green cartoon) highlights the flexibility of the regulatory and catalytic loops in the oxidized (disordered) state. Subsequent reduction breaks the disulfide bond, restoring the initial active state. This reversible redox mechanism enables the enzyme to adapt dynamically to fluctuations in the redox environment. The mannose positioned in the −1 subsite of the active enzyme was obtained by structural superposition with *Dt*Man (PDB 5N6U[23]).

metabolism occur in the periplasm[42], a compartment characterized by inherent redox gradients[43]. Such an environment provides a natural context for redox-sensitive regulation, enabling dynamic control of enzymatic activity in response to biotic and abiotic stress. Notably, intracellular redox homeostasis is highly dynamic, involving dedicated systems, such as thiol-disulfide oxidoreductases (e.g., DsbA/DsbC)[44] and glutathione-dependent pathways[3], which catalyze the reversible formation or reduction of disulfide bonds in target proteins. These systems, combined with local H_2O_2 microgradients, could modulate CapGH2b activity through coupled oxidation/reduction cycles that are not fully captured in in vitro experiments.

The discovery of such redox switch mechanism in the superfamily of glycoside hydrolases expands our understanding of microbial carbohydrate metabolism under oxidative environments, paving the way for future studies on redox-regulated carbohydrate enzymology, which is relevant for biocatalytic processes in nature and biotechnology.

Methods

SSN and phylogenetic analyses

SSN and phylogenetic analyses were conducted using a set of CapGH2b homologous retrieved from a local version of the CAZy database, built on NCBI NR (accessed August 2024), and from the UniProt database (accessed January 2025). For local searches, DIAMOND v2.1.9.163[45] was employed, retaining sequences with ≥30% identity to CapGH2b and an e-value $< 1 \times 10^{-10}$. BLAST search against UniProt database was additionally used to retrieve the top 250 hits with the same thresholds (≥30% identity; e-value $< 1 \times 10^{-10}$). To complement this dataset, ten sequences containing conserved cysteine residues were manually added, along with 215 functionally characterized GH2 sequences from the CAZy database[46]. Redundancy was subsequently reduced using CD-HIT v4.8.1[47] to remove identical entries, yielding a final curated dataset of 335 proteins.

SSN analyses were performed using the web-based Enzyme Function Initiative-Enzyme Similarity Tool[48]. The initial SSN was constructed by setting the edge calculation parameter as an e-value of 1e-10 and an alignment score of 147. The SSN was analyzed using Cytoscape[49]. Additional filters to remove edges below 35% identity and clusters with fewer than 16 nodes were applied. The final SSN was represented with an organic layout, and the resulting clusters were colored based on characterized GH2's enzyme commission (EC), according to the CAZy database.

For phylogenetic inference, a multiple sequence alignment was generated using MAFFT (v7.490)[50], with the parameters −genefpair and −maxiterate 1000. After alignment inspection, IQ-TREE2 (v2.2.2.7)[51] was employed to reconstruct the phylogenetic tree −B 1000 and −m MFP settings. The resulting tree was visualized in iTOL[52], incorporating EC annotations from characterized GH2, and branches with ultrafast bootstrap support below 95 were removed.

Mutagenesis, protein expression, and purification

The sequence encoding CapGH2b cloned into pET-28a(+) vector with the N-terminal 6×HisTag, and containing codon optimized for *Escherichia coli* expression, was synthesized by GenScript. Site-directed mutagenesis of C427A, C517A, C427A/C517A, E465A and E553Q variants was performed using the QuickChange II XL Site-Directed Mutagenesis Kit (Agilent Technologies). The primer pairs employed for each mutation are detailed in Supplementary Table 7 and were chemically synthesized by Exxtend.

Each vector (WT and variants) was transformed into *E. coli* BL21(DE3) cells by heat shock and grown in auto-induction medium (1% tryptone and 0.5% yeast extract) containing 2 mM magnesium sulfate and kanamycin (100 mg mL^{-1}), and 2% of solutions B (25 mM disodium hydrogen phosphate, 25 mM potassium dihydrogen phosphate, 50 mM ammonium chloride, 5 mM sodium sulfate) and C (0.5% glycerol, 0.05% glucose, 0.2% lactose) at 37 °C, 200 rpm for 5 h. Then, incubation was continued at 18 °C, 180 rpm for 16 h. The cells were harvested by centrifugation at 4 °C, 7500 *g* for 15 min, and then resuspended in buffer A (20 mM sodium phosphate pH 7.4, 500 mM sodium chloride, 5 mM imidazole) containing 4 mM phenylmethylsulfonyl fluoride (PMSF), 0.1 mg mL^{-1} lysozyme and 0.05 mg mL^{-1} DNAse for lysis by sonication.

The lysed cells were clarified by centrifugation (4 °C, 30,000 *g* for 1 h) and the supernatant was loaded onto a 5 mL HiTrap Chelating HP column (GE Healthcare Biosciences) pre-equilibrated with buffer A, coupled to an ÄKTA system (GE Healthcare Biosciences). A nonlinear gradient of buffer B (20 mM sodium phosphate pH 7.4, 500 mM sodium chloride, and 500 mM imidazole) was used for protein elution. The eluted fractions were analyzed by SDS–PAGE under denaturing conditions[53]. The selected samples were pooled, concentrated by filtration, and submitted to size-exclusion chromatography (SEC) using a Superdex 200 16/60 column (GE Healthcare Biosciences) pre-equilibrated with 20 mM sodium phosphate pH 7.4, 150 mM NaCl, at a flow rate of 1 mL min^{-1}. CapGH2b concentration was estimated measuring the absorbance at 280 nm, using the molecular weight and the extinction coefficient.

Enzyme assays

The CapGH2b activity was screened against polysaccharides and synthetic substrates (ρ-nitrophenyl conjugates) (Supplementary Table 8). The assays were performed using 2 mg mL^{-1} of the enzyme, 150 mM McIlvaine buffer pH 5.0, and 0.5% (*w/v*) of polysaccharides or 5 mM of synthetic substrates (at final concentrations) at 40 °C for 16 h. For polysaccharides, the amount of reducing sugar released was determined using the DNS method (absorbance at 540 nm)[54], while the hydrolysis synthetic ρ-nitrophenyl substrates (Sigma–Aldrich) was determined by the release of ρ-nitrophenolate ion (absorbance at 410 nm) using an Infinite M200 Pro (Tecan) with i-Control v.1.10.4.0 software. Graphs were plotted using OriginPro 2025.

The optimum pH and temperature were determined using 10 μg enzyme, 5 mM ρnp-β-mannopyranoside, 75 mM McIlvaine buffer ranging pH from 2.0 to 8.0, and temperature from 10 °C to 70 °C, for 30 min. Enzyme response to ions was determined using 5 mM ions, 75 mM MES buffer pH 5.0, 3 mM ρnp-β-mannopyranoside, and 20 μg CapGH2b at 40 °C for 15 min. The substrate saturation curve was obtained using the enzyme concentration and reaction time in the linear range and under optimum pH and temperature conditions.

Inhibition assays were conducted using 100 mM monosaccharides (mannose, glucose, galactose, arabinose, xylose, and N-acetylglucosamine) in enzymatic reactions containing 75 mM McIlvaine buffer pH 5.0, 3 mM ρnp-β-mannopyranoside, and 20 μg CapGH2b at 40 °C for 15 min. The enzymatic response to dithiothreitol (DTT) was performed through CapGH2b (WT and C517A, 1 mg mL^{-1}, in 20 mM sodium phosphate pH 7.5 and 150 mM NaCl) incubation with 20 mM DTT at 25 °C, 300 rpm, during 10 min. Subsequently, 9.5 μg of treated enzyme was used in the enzymatic reaction containing 75 mM McIlvaine buffer pH 5.0 and 6 mM ρnp-β-mannopyranoside at 40 °C during 20 min.

For reducing kinetics, CapGH2b samples (WT and C517A) were previously subjected to mild oxidation (at 4 °C for 200 days). Oxidized samples (1 mg mL^{-1}, in 20 mM sodium phosphate pH 7.5 and 150 mM NaCl) were incubated with varying DTT concentration and incubation time, at 25 °C, 300 rpm. Following incubation, 9.5 μg of treated enzyme was used in the enzymatic reaction containing 75 mM McIlvaine buffer pH 5.0 and 6 mM ρnp-β-mannopyranoside at 40 °C, 20 min.

For peroxide oxidation, CapGH2b samples (WT, C517A, C427A and C427A/C517A 1 mg mL^{-1}, in 20 mM sodium phosphate pH 7.5 and 150 mM NaCl) were incubated with 50, 100, 250, or 500 μM of peroxide at 25 °C, 300 rpm. Aliquots were collected after 24 h and/or 48 h of incubation, treated with 2 μg catalase (Sigma–Aldrich) at 25 °C for 5 min to remove the peroxide excess, and subsequently incubated with 20 mM DTT at 25 °C, 300 rpm for 10 min. Enzymatic activities were assessed both after peroxide treatment and following 20 mM DTT or 2 mM TCEP incubation using 75 mM McIlvaine buffer pH 5.0 containing 6 mM ρnp-β-mannopyranoside, and 10 μg and 8.5 μg of CapGH2b, respectively, at 40 °C for 20 min.

Biophysical characterization by circular dichroism (CD)

CD experiments were carried out on a JASCOJ-815 spectropolarimeter equipped with a Peltier temperature controller (Jasco) to acquire measurements in the far UV (195–260 nm) at 20 °C, 100 nm min^{-1}, with 20 accumulations. The samples of CapGH2b WT and C517A variant (at 1 mg mL^{-1}) were previously incubated with 20 mM of DTT at 25 °C, 300 rpm, for 10 min or with 50, 100, 250, or 500 μM of peroxide at 25 °C, 300 rpm, for 24 h. The DTT excess was removed by filtration. Samples were prepared at a final concentration of 0.3 mg mL^{-1} in 2.4 mM sodium phosphate pH 7.4, and 18 mM sodium chloride. Thermal denaturation was performed with a heating rate of 1 °C min^{-1} and was monitored at 220 nm.

Hydrodynamic and oligomeric properties in solution

Size-exclusion chromatography coupled to multi-angle light scattering (SEC-MALS) experiments were performed using an Optilab refractive index monitor and 8-angle static light scattering detector DAWN 8 (Wyatt Technology). Detectors were coupled to Agilent 1260 Infinity II Isocratic Pump and Vialsampler (Agilent Technology) with a WTC-030N5 analytical size-exclusion column (Wyatt Technology). A total of 100 μL of CapGH2b WT, C517A or C427A (1 mg mL^{-1}), previously treated under oxidizing or reducing conditions, was loaded onto the column pre-equilibrated with 20 mM sodium phosphate pH 7.5 and 150 mM NaCl in a flow rate of 0.5 mL min^{-1}. SEC column was calibrated using BSA as a molecular weight marker, and data was processed using the ASTRA software 8.1.2 (Wyatt Technology).

Small-angle X-ray scattering (SAXS) measurement was performed at the SAXS1 beamline, LNLS (Campinas, Brazil), using a monochromatic X-ray beam (1.488 Å) (Supplementary Table 9). The X-ray scattering was recorded using a Pilatus 300 K (Dectris). The sample-to-detector distance was adjusted to a scattering-vector range of $0.01 < q < 0.5$ Å^{-1}, where q is the magnitude of the q-vector defined by $q=4\pi\sin\theta/\lambda$, and 2θ is the scattering angle. The CapGH2b sample at 7.6 mg mL^{-1} was prepared in 20 mM HEPES pH 7.4 and 150 mM sodium chloride buffer. Ten successive images of 30 seconds were recorded and used for calculations after subtracting the sample-buffer scattering. The molecular weight was estimated directly from the SAXS data using SAXSMoW[55]. The distribution curve *P(r)* was calculated using the GNOM package[56] and was used to estimate the radius of gyration (R_g). The molecular envelope was calculated from the experimental SAXS data using DAMMIN[57]. The theoretical scattering curve of the crystallographic structure, calculated using CRYSOL[58], was fitted into the SAXS molecular envelope using the program SUPCOMB[59].

Structure determination by X-ray crystallography

Crystals of CapGH2b wild-type (WT) and variants E465A and E553Q were grown by sitting-drop or hanging-drop vapor-diffusion method at 18 °C in drops containing the equivalent volume of protein and crystallization condition, detailed in Supplementary Table 2.

X-ray diffraction data were collected at the W01B-MX2 beamline of the Brazilian Synchrotron Radiation Light Laboratory (LNLS, Brazil), the BL9-2 beamline from the Stanford Synchrotron Radiation Light source (Stanford, CA), and at the MANACÁ beamline of Sirius (LNLS, Brazil). Data were indexed, integrated, and scaled using the XDS package[60]. The crystal structure was solved using the single-wavelength anomalous diffraction (SAD) method. The positions of selenium sites using the anomalous differences were obtained with SHELXD[61]. Phases were calculated using SHELXE[61], and the initial model was built using Buccaneer[62]. The atomic coordinates were refined with PHENIX.REFINE[63], alternating manual modeling and inspection cycles using COOT[64]. The refined models were validated with MolProbity server[65]. Processing and structure-refinement statistics are shown in Supplementary Table 1.

Structure determination by cryo-electron microscopy

The fresh (reduced) and long-term incubation (oxidized) samples from SEC were submitted to grids preparation for cryo-EM at 0.25 mg mL^{-1} (in 20 mM sodium phosphate pH 7.4, 150 mM NaCl). The grids were glow-discharged for 50 s with 25 mA at 0.37 mbar using Pelco EasiGlow glow-discharge and prepared using Vitrobot Mark IV (Thermo Fisher Scientific) operated at 22 °C and 100% humidity. 3 μL of samples were deposited in Quantifoil R 2/2 mesh 200 (Quantifoil), blotted for 4 s, and fast vitrified in liquid ethane. Data collections were performed at the Brazilian Nanotechnology National Laboratory, on a transmission electron microscope Titan Krios G3i (Thermo Fisher Scientific), operating at 300 kV with ×96,000 of magnification, which corresponds to a sampling of 0.67 Å per pixel. Movies were acquired using the software EPU 2.12.1 (Thermo Fisher Scientific) using a Falcon 3EC direct detector, operating in counting mode with 30 frames per movie, and an accumulated dose of 50 e$^-$ Å^{-2}, applying a defocus range from −1.3 to −2.8 μm.

A total of 3543 (reduced) and 3792 (oxidized) movies were imported to cryoSPARC v4.3.0[66] to perform the motion and CTF corrections. The initial round of particle picking using blob picker resulted in 10,117 (reduced) and 107,708 (oxidized) selected and extracted particles (box size 400 px, Fourier crop box size 200 px), aiming to obtain initial 2D classes, that were followed used for the template picker. The resulting 398,599 (reduced) and 760,934 (oxidized) particles, were selected and extracted (box size 400 px, Fourier crop box size 200 px) to follow 2D classification, with the blurred 2D classes discarded. The remaining 230,960 (reduced) and 300,249 (oxidized) particles were used for ab initio reconstructions, followed by homogeneous and non-uniform refinements.

Local motion correction and local and global CTF refinements were performed to improve the map quality. The global resolutions reported used the FSC method (cutoff of 0.143), achieving 2.62 Å (reduced) and 3.41 Å (oxidized). The final map was sharpened using DeepEMhancer[67]. The trimeric structure of CapGH2b obtained by X-ray crystallography was used as a template for loops reconstruction in COOT[64]. The models were refined by several series of real-space refinement in Phenix[63] and visual inspection and model optimization in COOT[64].

Molecular docking and molecular dynamics simulations

Molecular docking was conducted using Autodock Vina 1.1.2[68]. The ρnp-β-mannopyranoside and mannobiose ligands were docked into the active cryo-EM structure of CapGH2b within a grid box measuring 14 × 14 x 14 Å^3, centered at the midpoint of NH groups from residues W199 and W532 (x = 183.5 Å, y = 140.4 Å, z = 155.2 Å). The resulting monomeric structure of the Michaelis complex was replicated in all protomers by structural superimposition.

Simulations of the oxidized state of CapGH2b were carried out considering catalytic and regulatory loops modeled using Rosetta 3.10[69], and the intramolecular disulfide bond between C427 and C517 residues of all protomers was built using *tleap* utilitary from AmberTools 20[70,71]. The protonation state of all residues was determined at pH 5.0 using PROPKA 3.0[29]. Additionally, the protonation state of all His residues was evaluated by visual inspection based on their chemical environment. Classical molecular dynamics simulations were performed using the cuda-enabled PMEMD module of Amber 20 molecular dynamics package[70,71]. The system was prepared by retaining all crystallographic waters, and the trimeric structure was solvated in a water box ensuring a 15 Å padding from the protein atoms to the edges of the simulation box (Supplementary Table 10). The total charge of the system was neutralized by adding 24 sodium ions. In all simulations, the FF14SB forcefield was used to describe the protein, along with the TIP3P model for water molecules and GAFF parameters for ions.

Resulting simulation box was subjected to an initial energy minimization procedure with position restraints potential applied only to the protein structure. The system was further relaxed with an additional minimization procedure without restrictions. Several MD equilibration steps using a 1 fs timestep were performed as follows: i) the initial heating stage was performed through four consecutive NVT runs of 50 ps each. The first run was conducted at 100 K with restraints applied to all atoms except for water molecules and ions. The subsequent three runs were carried out without restraints at 100 K, 200 K and 313 K; ii) the density was equilibrated with a short 200 ps simulation at the NpT ensemble, followed by iii) final equilibration with another 200 ps simulation at NVT ensemble. Finally, the time step was increased to 2 fs, and productive simulations of 500 ns were performed using the SHAKE[72] algorithm. All MD data were analyzed by CPPTRAJ software from AmberTools 20[70,71] and VMD 1.9.3[73]. The generated molecular trajectories were visualized using VMD 1.9.3[73] and PyMOL (The PyMOL Molecular Graphics System, Version 3.0 Schrödinger, LLC).

Cysteine labeling

Controls of non-oxidized samples (200 μg of WT and C517A variant) were performed by alkylation using iodoacetamide (IAA) or *N*-ethylmaleimide (NEM). For that, initial reduction and denaturation were performed using 50 mM dithiothreitol (DTT) in 25 mM ammonium bicarbonate, pH 7.8 (ABC) with 5% (*w/v*) sodium deoxycholate (SDC) at 60 °C for 30 min. Reduced samples were transferred to a 0.5 mL Amicon filter (30 kDa MWCO, Merck Millipore) pre-passivated overnight with 1% (*v/v*) TWEEN-20, then centrifuged at 13,910 *g* for 20 min at 20 °C. After discarding the flowthrough, samples were washed three times with 450 μL of 8 M urea in 25 mM ABC buffer, and once with 25 mM ABC.

For IAA alkylation, 450 μL of IAA 50 mM was added and incubated at 25 °C for 50 min (in the dark), followed by 5 desalting centrifugation washes with 25 mM ABC at 13,910 *g*, 20 °C for 5 min. Trypsin was then added at a 1:25 *w/w* ratio for overnight digestion at 37 °C. Peptides were collected in the flowthrough after centrifugation at 13,910 *g*, 20 °C for 5 min, and dried.

Alkylation with NEM was performed after urea washes. For that, one washing step with 450 μL of 100 mM phosphate buffer pH 6.0 was performed and then, 450 μL of 50 mM NEM (in the same buffer) was added for alkylation at 25 °C for 2 h. The desalting washes, trypsin digestion and peptide collection steps were performed in the same manner as for IAA.

For the differential cysteine labeling, 200 μg of WT and C517A variant were oxidized with 500 μM peroxide at 25 °C, 300 rpm, for 24 h. Samples were then denatured with 5 % (*w/v*) SDC in 25 mM ABC at

60 °C for 30 min. After, samples were cooled down and IAA added to a final concentration of 50 mM, followed by incubation at 25 °C for 50 min (in the dark). Samples were transferred to a MWCO filter, centrifuged, and 450 μL of 50 mM DTT was added for incubation at 37 °C, 45 min. Subsequently, samples were washed 3 times with 8 M urea in 25 mM ABC buffer. Buffer was exchanged to 100 mM phosphate pH 6.0 by centrifugation 13,910 *g* at 20 °C for 20 min, and then, 450 μL of 50 mM NEM (in the same buffer) was added for alkylation at 25 °C for 2 hrs[74]. The desalting washes, trypsin digestion and peptide collection steps were performed as previously described for the standard curves. Both WT and variant C517A samples were initially separately and processed in triplicate. Peptides were either diluted or analyzed directly, starting from 150 pmol, and quantification values were then expressed as a percentage of 150 pmol.

Untargeted and targeted proteomics

Both untargeted and targeted proteomics were performed using a Synapt XS (Waters) coupled to ACQUITY Premier UPLC (Waters). The capillary voltage was set to 2.5 kV, the sampling cone to 25 V, source temperature to 120 °C, desolvation temperature to 500 °C, desolvation gas flow to 650 L h^{-1}, cone gas flow to 50 L h^{-1}, and nebulizer pressure to 6.5 bar. Data acquisition was carried out with MassLynx v.4.2. Mobile phases A and B consisted of 0.1 % (*v/v*) formic acid (A) and acetonitrile with 0.1% (*v/v*) formic acid (B), respectively. Peptide separation was performed using a peptide CSH column (1 mm × 100 mm, 1.7 μm, 130 Å) with a 4–35% gradient over 15 min at a flow rate of 50 μL min^{-1}. The gradient was followed by a 5 min wash with 95% B. Column equilibration with 4% B was carried out during the first and last 5 min of the run.

Untargeted ion mobility mass spectrometry with data-independent acquisition mode ($HDMS^E$, Waters) was used (50–2000 *m/z*, 0.5 s scan cycle), with a low collision energy of 6 eV and a ramped collision energy from 15 to 50 eV. Lock mass correction was applied every 30 s using the peptide standard leucine-enkephalin (100 pg $μL^{-1}$) within a mass window of 0.5 Da.

Data processing was performed in Progenesis QI for Proteomics 4.2 (Nonlinear Dynamics), applying a 1% false discovery rate, 20 ppm for MS1 error tolerance, and automatic MS2 error adjustment. Protein identification required at least two unique peptides, each supported by a minimum of three fragment ions. The protein database used for identification included the complete *E. coli* proteome (downloaded from UniProt on January 22, 2024) supplemented with the sequence of the recombinant protein analyzed in this study. Protein was digested with trypsin, allowing up to two missed cleavages at K/R sites, except when followed by proline. Methionine oxidation was set as a variable modification. For controls labeled with IAA or NEM, carbamidomethylation or NEM modification of cysteine was set as a fixed modification, respectively. In contrast to that, cysteine modification with IAA or NEM was set as variable for oxidized samples differentially labeled. Additionally, searches were performed with sulfinic and sulfonic acids as variable cysteine modifications. Label-free quantification was performed using normalized abundance values calculated in Progenesis, based on the sum of intensities within isotope boundaries.

Targeted proteomics data were acquired in a Synapt XS (Waters) using ion mobility mass spectrometry coupled to multiple reaction monitoring (HD-MRM, Waters), with RADAR (Waters) scanning every 5 s. A 0.5 s scan cycle was used with low collision energy of 6 eV. Parameters of targeted analysis are described in Supplementary Tables 5 and 6. Separate standard curves for IAA or NEM were generated using serial dilutions, starting from 150 pmol of peptides. Linear response for control standard curves quantification is demonstrated on Supplementary Fig. 17. Lock mass standard was applied every 30 s using the peptide leucine-enkephalin (100 pg $μL^{-1}$). Post-processing of continuous lock mass correction was performed using the accurate mass measurement tool in MassLynx 4.2, applying an average of three scans within a mass window of 0.5 Da. Extracted ion chromatograms (20 ppm) and peak integration were done on TargetLynx v 4.2, with Apex Track tool enabled, peak-to-peak baseline threshold of 4 and smoothing by the mean method with 4 iterations. The raw data for mass spectra are detailed in Supplementary Data.

Inclusion and ethics statement

All researchers who fulfilled the authorship criteria of Nature Portfolio journals are included in the author list. Contributions included the design, execution, and interpretation of the study, with roles and responsibilities defined and mutually agreed upon by all collaborators. This research was conducted without restrictions and in a manner that avoids stigmatization, incrimination, or discrimination of any individual or group. We are committed to the inclusive, diverse, and equitable conduct of research.

Reporting summary

Further information on research design is available in the Nature Portfolio Reporting Summary linked to this article.

Data availability

The cryo-EM maps have been deposited in the Electron Microscopy Data Bank (EMDB) under accession codes EMD-49363 (oxidized CapGH2b map) and EMDB-49364 [https://www.ebi.ac.uk/pdbe/entry/emdb/EMD-49364] (reduced CapGH2b structure and map). The atomic coordinates have been deposited in the Protein Data Bank (PDB) under accession codes 9NFE (reduced CapGH2b structure), 9NP8 (oxidized CapGH2b structure, space group I213); 9NP9 (oxidized CapGH2b structure – E553Q variant, space group I213); 9NPA (oxidized CapGH2b structure, space group I213); 9NPB (oxidized CapGH2b structure, space group R3); 9NPC (oxidized CapGH2b structure, space group I212121); 9NPD [EMD-] (oxidized CapGH2b structure – E553Q variant, space group P3121); 9NPE (oxidized CapGH2b structure, space group P1); 9NPF (oxidized CapGH2b structure, space group P1); 9NPL (oxidized CapGH2b structure – E553Q variant, space group P1); and 9NPN (oxidized CapGH2b structure – E465A variant, space group P1). The molecular dynamics simulations and SAXS datasets have been deposited at Zenodo [https://doi.org/10.5281/zenodo.17494902]. The MD files include the topology file used in the MD simulations, input file for production runs of MD simulations, and the initial and final coordinates files from production. SAXS files include the merged experimental SAXS scattering curve obtained for CapGH2b, output file generated by ATSAS package, theoretical scattering curve generated by CRYSOL, and the molecular envelope obtained using DAMAVER. The mass spectrometry proteomics data have been deposited to the ProteomeXchange Consortium via the PRIDE partner repository with the dataset identifier PXD070002. Previously published atomic coordinates from the Protein Data Bank (PDB accession codes 5N6U, 2JE8, 6BYE, and 4CVU) were used for structural comparison. Other data generated or analyzed during this study are included in the published article and its Supplementary Information files. Source data are provided with this paper.

References

1. Cremers, C. M. & Jakob, U. Oxidant sensing by reversible disulfide bond formation. *J. Biol. Chem.* **288**, 26489–26496 (2013).
2. Mora, M. et al. A single-molecule strategy to capture non-native intramolecular and intermolecular protein disulfide bridges. *Nano Lett.* **22**, 3922–3930 (2022).
3. Wouters, M. A., Fan, S. W. & Haworth, N. L. Disulfides as redox switches: from molecular mechanisms to functional significance. *Antioxid. Redox Signal.* **12**, 53–91 (2010).
4. Choi, H. et al. Structural basis of the redox switch in the OxyR transcription factor. *Cell* **105**, 103–113 (2001).

5. Kemble, D. J. & Sun, G. Direct and specific inactivation of protein tyrosine kinases in the Src and FGFR families by reversible cysteine oxidation. *Proc. Natl. Acad. Sci. USA* **106**, 5070–5075 (2009).
6. Rutkiewicz, M., Bujacz, A., Wanarska, M., Wierzbicka-Wos, A. & Cieslinski, H. Active site architecture and reaction mechanism determination of cold-adapted (β-D-galactosidase from *Arthrobacter* sp. 32cB. *Int. J. Mol. Sci*. **20**, 4301 (2019).
7. Pereira-Rodríguez, Á. et al. Structural basis of specificity in tetrameric *Kluyveromyces lactis* β-galactosidase. *J. Struct. Biol.* **177**, 392–401 (2012).
8. Ellinghaus, T. L. et al. Engineering glycoside hydrolase stability by the introduction of zinc binding. *Acta Crystallogr. Sect. D. Struct. Biol.* **74**, 702–710 (2018).
9. Maruyama, S. et al. Substrate complex structure, active site labeling and catalytic role of the zinc ion in cysteine glycosidase. *Glycobiology* **32**, 171–180 (2022).
10. McGregor, N. G. S. et al. Cysteine Nucleophiles in Glycosidase Catalysis: Application of a Covalent β-L-arabinofuranosidase Inhibitor. *Angew. Chem.* **133**, 5818–5822 (2021).
11. Rajan, S. S. et al. Novel catalytic mechanism of glycoside hydrolysis based on the structure of an NAD$^+$/Mn^{2+}-dependent phospho-α-glucosidase from *Bacillus subtilis*. *Structure* **12**, 1619–1629 (2004).
12. Kim, H. W. & Ishikawa, K. The role of disulfide bond in hyperthermophilic endocellulase. *Extremophiles* **17**, 593–599 (2013).
13. Okano, H. et al. Structure and stability of metagenome-derived glycoside hydrolase family 12 cellulase (LC-CelA) a homolog of Cel12A from *Rhodothermus marinus*. *FEBS Open Bio* **4**, 936–946 (2014).
14. Yang, H. et al. Impact of disulfide bonds on the folding and refolding capability of a novel thermostable GH45 cellulase. *Appl. Microbiol. Biotechnol.* **102**, 9183–9192 (2018).
15. Cheng, Y. S. et al. Structural analysis of a glycoside hydrolase family 11 xylanase from *Neocallimastix patriciarum*: Insights into the molecular basis of a thermophilic enzyme. *J. Biol. Chem.* **289**, 11020–11028 (2014).
16. Muttathukattil, A. N., Singh, P. C. & Reddy, G. Role of Disulfide Bonds and Topological Frustration in the Kinetic Partitioning of Lysozyme Folding Pathways. *J. Phys. Chem. B* **123**, 3232–3241 (2019).
17. Wetzel, R., Perry, L. J., Baase, W. A. & Becktel, W. J. Disulfide bonds and thermal stability in T4 lysozyme. *Proc. Natl. Acad. Sci. USA* **85**, 401–405 (1988).
18. Santos, C. A. et al. A metagenomic 'dark matter' enzyme catalyses oxidative cellulose conversion. *Nature* **639**, 1–8 (2025).
19. Cabral, L. et al. Gut microbiome of the largest living rodent harbors unprecedented enzymatic systems to degrade plant polysaccharides. *Nat. Commun.* **13**, 629 (2022).
20. Vieira, P. S. et al. Xyloglucan processing machinery in *Xanthomonas* pathogens and its role in the transcriptional activation of virulence factors. *Nat. Commun.* **12**, 4049 (2021).
21. Lebreton, A. et al. Division of the large and multifunctional glycoside hydrolase family 2: high functional specificity and biochemical assays in the uncharacterized subfamilies. *Biotechnol. Biofuels Bioprod.* **18**, 68 (2025).
22. Tailford, L. E. et al. Mannose foraging by *Bacteroides thetaiotaomicron*: Structure and specificity of the β-mannosidase, *Bt*Man2A. *J. Biol. Chem.* **282**, 11291–11299 (2007).
23. Guillotin, L., Richet, N., Lafite, P. & Daniellou, R. Is the acid/base catalytic residue mutation in β-D-mannosidase *Dt*Man from *Dictyoglomus thermophilum* sufficient enough to provide thioglycoligase activity? *Biochimie* **137**, 190–196 (2017).
24. Prilusky, J. et al. FoldIndex©: A simple tool to predict whether a given protein sequence is intrinsically unfolded. *Bioinformatics* **21**, 3435–3438 (2005).
25. Domingues, M. N. et al. Structural basis of exo-β-mannanase activity in the GH2 family. *J. Biol. Chem.* **293**, 13636–13649 (2018).
26. Martins, M. P. et al. Glycoside hydrolase subfamily GH5_57 features a highly redesigned catalytic interface to process complex hetero-β-mannans. *Acta Crystallogr. Sect. D. Struct. Biol.* **78**, 1358–1372 (2022).
27. Nascimento, A. S., Muniz, J. R. C., Aparício, R., Golubev, A. M. & Polikarpov, I. Insights into the structure and function of fungal β-mannosidases from glycoside hydrolase family 2 based on multiple crystal structures of the *Trichoderma harzianum* enzyme. *FEBS J.* **281**, 4165–4178 (2014).
28. Beedle, A. E. M., Lynham, S. & Garcia-Manyes, S. Protein S-sulfenylation is a fleeting molecular switch that regulates non-enzymatic oxidative folding. *Nat. Commun.* **7**, 12490 (2016).
29. Olsson, M. H. M., Sondergaard, C. R., Rostkowski, M. & Jensen, J. H. PROPKA3: consistent treatment of internal and surface residues in empirical pKa calculations. *J. Chem. Theory Comput.* **7**, 525–537 (2011).
30. Chiu, J. & Hogg, P. J. Allosteric disulfides: sophisticated molecular structures enabling flexible protein regulation. *J. Biol. Chem.* **294**, 2949–2960 (2019).
31. Fan, S. W. et al. Conformational changes in redox pairs of protein structures. *Protein Sci.* **18**, 1745–1765 (2009).
32. Littler, D. R. et al. The intracellular chloride ion channel protein CLIC1 undergoes a redox-controlled structural transition. *J. Biol. Chem.* **279**, 9298–9305 (2004).
33. Mizohata, E. et al. Crystal structure of an archaeal peroxiredoxin from the aerobic hyperthermophilic crenarchaeon *Aeropyrum pernix* K1. *J. Mol. Biol.* **354**, 317–329 (2005).
34. Reinke, P. Y. A. et al. SARS-CoV-2 Mpro responds to oxidation by forming disulfide and NOS/SONOS bonds. *Nat. Commun. 2024* **15**, 1–10 (2024).
35. Funk, L. M. et al. Multiple redox switches of the SARS-CoV-2 main protease in vitro provide opportunities for drug design. *Nat. Commun. 2024* **15**, 1–18 (2024).
36. Xu, L., Benson, S. D., Butcher, S. J., Bamford, D. H. & Burnett, R. M. The receptor binding protein P2 of PRD1, a virus targeting antibiotic-resistant bacteria, has a novel fold suggesting multiple functions. *Structure* **11**, 309–322 (2003).
37. Oubrie, A., Rozeboom, H. J., Kalk, K. H., Duine, J. A. & Dijkstra, B. W. The 1.7 Å crystal structure of the apo form of the soluble quinoprotein glucose dehydrogenase from *Acinetobacter calcoaceticus* reveals a novel internal conserved sequence repeat. *J. Mol. Biol.* **289**, 319–333 (1999).
38. Oubrie, A. et al. Structure and mechanism of soluble quinoprotein glucose dehydrogenase. *EMBO J.* **18**, 5187–5194 (1999).
39. Lincecum, T. L. et al. Structural and mechanistic basis of pre- and posttransfer editing by leucyl-tRNA synthetase. *Mol. Cell* **11**, 951–963 (2003).
40. Cusack, S., Yaremchuk, A. & Tukalo, M. The 2 Å crystal structure of leucyl-tRNA synthetase and its complex with a leucyl-adenylate analogue. *EMBO J.* **19**, 2351–2361 (2000).
41. Yu, C.-S., Chen, Y.-C., Lu, C.-H. & Hwang, J.-K. Prediction of protein subcellular localization. *Proteins Struct. Funct. Bioinf.* **64**, 643–651 (2006).
42. McKee, L. S. et al. Polysaccharide degradation by the Bacteroidetes: mechanisms and nomenclature. *Environ. Microbiol. Rep.* **13**, 559–581 (2021).
43. Cho, S. H. & Collet, J. F. Many roles of the bacterial envelope reducing pathways. *Antioxid. Redox Signal.* **18**, 1690–1698 (2013).
44. Dutton, R. J., Boyd, D., Berkmen, M. & Beckwith, J. Bacterial species exhibit diversity in their mechanisms and capacity for protein disulfide bond formation. *Proc. Natl. Acad. Sci. Usa.* **105**, 11933–11938 (2008).

45. Buchfink, B., Reuter, K. & Drost, H. G. Sensitive protein alignments at tree-of-life scale using DIAMOND. *Nat. Methods* **18**, 366–368 (2021).
46. Drula, E. et al. The carbohydrate-active enzyme database: Functions and literature. *Nucleic Acids Res* **50**, D571–D577 (2022).
47. Li, W. & Godzik, A. Cd-hit: A fast program for clustering and comparing large sets of protein or nucleotide sequences. *Bioinformatics* **22**, 1658–1659 (2006).
48. Oberg, N., Zallot, R. & Gerlt, J. A. EFI-EST, EFI-GNT, and EFI-CGFP: enzyme function initiative (EFI) web resource for genomic enzymology tools. *J. Mol. Biol.* **435**, 168018 (2023).
49. Shannon, P. et al. Cytoscape: a software environment for integrated models of biomolecular interaction networks. *Genome Res.* **13**, 2498–2504 (2003).
50. Katoh, K. & Standley, D. M. MAFFT multiple sequence alignment software version 7: improvements in performance and usability. *Mol. Biol. Evol.* **30**, 772–780 (2013).
51. Minh, B. Q. et al. IQ-TREE 2: new models and efficient methods for phylogenetic inference in the genomic era. *Mol. Biol. Evol.* **37**, 1530–1534 (2020).
52. Letunic, I. & Bork, P. Interactive tree of life (iTOL) v6: recent updates to the phylogenetic tree display and annotation tool. *Nucleic Acids Res.* **52**, W78–W82 (2024).
53. Laemmli, U. K. Cleavage of structural proteins during the assembly of the head of bacteriophage T4. *Nature* **227**, 680–685 (1970).
54. Miller, G. L. Use of dinitrosalicylic acid reagent for determination of reducing sugar. *Anal. Chem.* **31**, 426–428 (1959).
55. de Oliveira Neto, M. et al. SAXSMoW 3.0: new advances in the determination of the molecular weight of proteins in dilute solutions from SAXS intensity data on a relative scale. *Protein Sci.* **31**, 251–258 (2022).
56. Svergun, D. I. Determination of the regularization parameter in indirect-transform methods using perceptual criteria. *J. Appl. Crystallogr.* **25**, 495–503 (1992).
57. Svergun, D. I. Restoring low resolution structure of biological macromolecules from solution scattering using simulated annealing. *Biophys. J.* **76**, 2879–2886 (1999).
58. Svergun, D., Barberato, C. & Koch, M. H. CRYSOL-A program to evaluate X-ray solution scattering of biological macromolecules from atomic coordinates. *J. Appl. Crystallogr.* **28**, 768–773 (1995).
59. Kozin, M. B. & Svergun, D. I. Automated matching of high- and low-resolution structural models. *J. Appl. Crystallogr.* **34**, 33–41 (2001).
60. Kabsch, W. Xds. *Acta Crystallogr. Sect. D. Biol. Crystallogr.* **66**, 125–132 (2010).
61. Sheldrick, G. M. Experimental phasing with SHELXC/D/E: combining chain tracing with density modification. *Acta Crystallogr. Sect. D. Biol. Crystallogr.* **66**, 479–485 (2010).
62. Cowtan, K. The Buccaneer software for automated model building. 1. Tracing protein chains. *Acta Crystallogr. Sect. D. Biol. Crystallogr.* **62**, 1002–1011 (2006).
63. Afonine, P. V. et al. Towards automated crystallographic structure refinement with phenix. Refine. *Acta Crystallogr. Sect. D. Biol. Crystallogr.* **68**, 352–367 (2012).
64. Emsley, P., Lohkamp, B., Scott, W. G. & Cowtan, K. Features and development of coot. *Acta Crystallogr. Sect. D. Biol. Crystallogr.* **66**, 486–501 (2010).
65. Williams, C. J. et al. MolProbity: more and better reference data for improved all-atom structure validation. *Protein Sci.* **27**, 293–315 (2018).
66. Punjani, A., Rubinstein, J. L., Fleet, D. J. & Brubaker, M. A. CryoSPARC: Algorithms for rapid unsupervised cryo-EM structure determination. *Nat. Methods* **14**, 290–296 (2017).
67. Sanchez-Garcia, R. et al. DeepEMhancer: a deep learning solution for cryo-EM volume post-processing. *Commun. Biol.* **4**, 1–8 (2021).
68. Trott, O. & Olson, A. J. AutoDock Vina: Improving the speed and accuracy of docking with a new scoring function, efficient optimization, and multithreading. *J. Comput. Chem.* **31**, 455–461 (2010).
69. Leaver-Fay, A. et al. Rosetta3: an object-oriented software suite for the simulation and design of macromolecules. *Methods Enzymol.* **487**, 545–574 (2011).
70. Case, D. A. et al. The Amber biomolecular simulation programs. *J. Comput. Chem.* **26**, 1668–1688 (2005).
71. Salomon-Ferrer, R. et al. Routine microsecond molecular dynamics simulations with AMBER on GPUs. 2. Explicit solvent particle mesh ewald. *J. Chem. Theory Comput.* **9**, 3878–3888 (2013).
72. Ryckaert, J. P., Ciccotti, G. & Berendsen, H. J. C. Numerical integration of the cartesian equations of motion of a system with constraints: molecular dynamics of n-alkanes. *J. Comput. Phys.* **23**, 327–341 (1977).
73. Humphrey, W., Dalke, A. & Schulten, K. V. M. D. Visual molecular dynamics. *J. Mol. Graph.* **14**, 33–38 (1996).
74. Fuzita, F., Ronsein, G. E. & Di Mascio, P. A simple and direct approach for cysteine-based redox proteomics by differential isobaric labeling validated in human and rat aortic smooth muscle cells. *Free Radic. Biol. Med.* **192**, 61 (2022).

Acknowledgements

We acknowledge the Brazilian Synchrotron Light Laboratory (LNLS) for the provision of time on the MANACÁ, MX2, and SAXS1 beamlines, the Brazilian Biosciences National Laboratory (LNBio) for the use of ROBOLAB facility, and Brazilian Biorenewables National Laboratory (LNBR) for the use of biophysics of macromolecules and multi-omics facilities. We acknowledge the National Nanotechnology Laboratory (LNNano) for the provision of time on the transmission electron microscopes JEM 1400 Plus (Jeol), Talos Arctica G2 (Thermo Fisher Scientific) and Titan Krios G3i (Thermo Fisher Scientific). We acknowledge the Stanford Synchrotron Radiation Lightsource (SSRL) at the SLAC National Accelerator Laboratory (Menlo Park, CA, USA) for access to beamline 9-2. We acknowledge the National Laboratory for Scientific Computing (LNCC/MCTI, Brazil) for providing HPC resources of the SDumont supercomputer, which have contributed to produce the simulations results. We thank Dr. Li Yu for valuable contribution in the biochemical data interpretation. This research was supported by grants from Fundação de Amparo à Pesquisa do Estado de São Paulo (grant no. 2021/04891-3 to M.T.M., 2022/03059-5 to G.F.P., 2021/09793-0 to M.P.M., 2024/15257-1 to G.H.M., 2022/06298-0 to J.P.M.S., and 2022/09386-8 to F.S.) and Conselho Nacional de Desenvolvimento Científico e Tecnológico (CNPq) (grant no. 303898/2024-0 to M.T.M. and 304440/2024-8 G.F.P.

Author contributions

M.P.M., G.F.P., M.A.B.M., and M.T.M. designed the study and wrote the paper. M.P.M., G.H.M., F.M.C., F.S., R.H.G., Y.Y., P.D., G.F.P., M.A.B.M., and M.T.M. contributed to data analyses and discussions. R.S.A.S. and G.F.P. performed the bioinformatic analyses. M.P.M. expressed, purified the enzymes and performed the functional characterization. M.P.M. and F.S. performed biophysical analyses. G.H.M., M.A.B.M., and F.M.C. performed the molecular dynamic simulations. F.J.F. designed and performed mass spectrometry analyses. M.P.M., J.P.M.S., R.Y.M., M.A.B.M., and M.T.M. collected, processed, refined, and analyzed the X-ray data. M.P.M., C.R.S., L.G.D., and A.C.B. prepared grids, collected and processed the cryo-EM data.

Competing interests

The authors declare no competing interests.

Additional information

Supplementary information The online version contains supplementary material available at https://doi.org/10.1038/s41467-025-67225-2.

Correspondence and requests for materials should be addressed to Mario Tyago Murakami.

Peer review information *Nature Communications* thanks Haishan Gao, Takatsugu Miyazaki and the other, anonymous, reviewer(s) for their contribution to the peer review of this work. A peer review file is available.

Reprints and permissions information is available at http://www.nature.com/reprints